https://doi.org/10.5194/egusphere-2026-2724
Preprint. Discussion started: 16 June 2026

A New NO_2 Profile Retrieval from a Combination of Scanning Long-Path DOAS and Point Measurements Using Bayesian Inference-Based Spatiotemporal Reconstructions

Manuel Henning[1], Philipp Haim[2], Stefan Schmitt[3], Johannes Lampel[3], Denis Pöhler[3], and Mark Wenig[1]

[1]Meteorological Institute, Ludwig-Maximilians-Universität, 80539 Munich, Germany
[2]Chair of Biological Imaging, Central Institute for Translational Cancer Research (TranslaTUM), School of Medicine and Health & School of Computation, Information and Technology, Technical University of Munich, 81675 München, Germany, Institute of Biological and Medical Imaging, Bioengineering Center, Helmholtz Zentrum München, 85764 Neuherberg, Germany, Institute of Computational Biology, Helmholtz Zentrum München, 85765 Neuherberg, Germany, Institute of AI for Health, Helmholtz Zentrum München, 85764 Neuherberg, Germany, and Ludwig-Maximilians-Universität, 80539 Munich, Germany
[3]Airyx GmbH, 69123 Heidelberg, Germany

Correspondence: Manuel Henning (manuel.henning@physik.lmu.de)

Abstract. This study presents a fully Bayesian approach for retrieving reliable vertical profiles of nitrogen dioxide (NO_2) from a combination of path and in-situ measurements. Instead of focusing on complete two-dimensional reconstructions, we employ a three-dimensional correlated field model (2D in space + 1D in time) as a physically consistent intermediary step to extract profile information. The Bayesian inference framework, implemented using the Numerical Information Field Theory for Python library (NIFTy), allows for a rigorous propagation of measurement uncertainties and explicitly includes spatial and temporal correlations. Data from the CINDI-III campaign, including two in-situ ICAD devices and a new DOAS system, were used as input. The new DOAS system consists of a fast scanning active and passive DOAS instrument that can be used for Long-Path as well as MAX-DOAS measurements, called HyDOAS (Hybrid Differential Optical Absorption Spectroscopy). The resulting profiles were compared against independent MAX-DOAS retrievals as a consistency check. Our results demonstrate that the Bayesian spatiotemporal framework yields physically consistent and temporally coherent NO_2 profiles that agree well with established methods within their uncertainties. The approach offers a promising pathway to derive high-quality vertical information even from geometrically limited measurement configurations.

1 Introduction

Nitrogen dioxide (NO_2) is a critical air pollutant that plays a significant role in atmospheric chemistry and has substantial impacts on human health and the environment. It is primarily produced by anthropogenic activities, including fossil fuel combustion in vehicles and industrial processes (Seinfeld and Pandis, 2016). Long-term exposure to NO_2 has been linked to respiratory issues, cardiovascular diseases, and increased mortality rates in urban areas (WHO, 2021; Faustini et al., 2014).

Various techniques are employed to measure NO_2 concentrations in the atmosphere, including in-situ methods and remote sensing approaches. Point measurement devices such as Iterative Cavity DOAS (ICAD) devices provide high-precision mea-

https://doi.org/10.5194/egusphere-2026-2724
Preprint. Discussion started: 16 June 2026

surements at specific locations (Horbanski et al., 2019). Long-Path Differential Optical Absorption Spectroscopy (LP-DOAS) is a remote sensing technique that allows for the measurement of atmospheric trace gases like NO_2 over extended distances, typically ranging from several hundred meters to a few kilometers, providing spatially averaged concentrations along the light path. Multi-Axis Differential Optical Absorption Spectroscopy (MAX-DOAS) has emerged as a powerful tool for retrieving vertical profiles of trace gases like NO_2 (Platt and Stutz, 2008). The main measurement device used in this study is a Hybrid DOAS (HyDOAS) device, developed by Airyx GmbH, able to measure in active (i.e. LP-DOAS), as well as passive (i.e. MAX-DOAS) mode.

Reconstructing the spatial and temporal dynamics of NO_2 is crucial to test current models or to monitor the air quality in general. Methods for the reconstruction of NO_2 distributions from incomplete measurement data include studies by Hartl (2007) and Laepple et al. (2004) which use discretized basis functions and least squares methods to solve the underlying underdetermined system with mixed results. A crucial disadvantage of such methods is that either unphysical assumptions concerning the prior model have to be made or that the error estimation basically comes down to a stability analysis of the reconstruction process.

We propose the use of a purely Bayesian framework to retrieve vertical NO_2 profiles from sparse and geometrically constrained measurements. In contrast to conventional tomographic approaches, we employ a generative correlated field model (Arras et al., 2021, 2022) to represent the spatiotemporal (2-dimensional in space and 1-dimensional in time) NO_2 distribution as a continuous field. This 2+1D formulation provides the physical consistency required to derive meaningful vertical gradients and boundary-layer structures, even when horizontal resolution is limited. Using the Numerical Information Field Theory framework (NIFTy) (Edenhofer et al., 2024; Arras et al., 2019; Steininger et al., 2019; Selig et al., 2013), we perform variational inference on this field, allowing uncertainty quantification and temporal coherence to be preserved in the resulting profiles. NIFTy contains accurate methods for variational inference (VI) and gaussian processes (Frank et al., 2021; Knollmüller and Enßlin, 2020). While NIFTy has been applied mainly in astrophysics and medical imaging, this is, to our knowledge, the first application of a generative correlated field model with full variational posterior inference in atmospheric trace-gas profiling.

Incorporating spatiotemporal correlations in atmospheric modeling is crucial for accurately representing the dynamic nature of air pollution. NIFTy's ability to include prior models with both spatial and temporal dependencies allows for a more comprehensive understanding of NO_2 distribution patterns over time and to bridge measurement gaps that arise from the sparse and geometrically constrained measurement networks.

To check this novel approach for consistency, we compare the NIFTy reconstructions with established methods such as MAX-DOAS profile retrievals. This comparison serves to evaluate the performance of our method in capturing NO_2 distributions. By conducting this analysis, we can identify the strengths and potential limitations of the NIFTy-based reconstructions, particularly in terms of spatial and temporal resolution improvements and uncertainty quantification.

This study aims to develop and validate a Bayesian framework for deriving vertical NO_2 profiles from limited path and in-situ observations. The specific objectives are to:

1. reconstruct correlated two-dimensional NO_2 fields as a physically consistent basis for vertical profile retrievals,

https://doi.org/10.5194/egusphere-2026-2724
Preprint. Discussion started: 16 June 2026

2. extract and evaluate 1D height profiles from these reconstructions, and

3. compare the resulting profiles with independent MAX-DOAS retrievals and with geometrically derived so called boxlayer estimates to assess consistency under simplified geometric assumptions.

Improved NO_2 monitoring techniques are crucial for effective urban air quality management and policy-making. This study's approach to spatiotemporal NO_2 distribution reconstruction has the potential to enhance our understanding of pollution dynamics. By providing temporally resolved 2D cross-sections of the near-surface NO_2 field, this research could contribute to better-informed decisions on emission control strategies and urban planning to mitigate air pollution impacts on public health.

This paper is structured as follows: Section 2 gives an overview of similar studies and motivates the need for a statistical inversion method. Section 3 describes the measurement techniques and post-processing of the data used in this study. Section 4 outlines the Bayesian Inference framework provided by NIFTy and the likelihood and prior setup. Inference - and Validation methods are described in section 5. Section 6 presents the results of our reconstructions. Section 7 contains the comparisons with MAX-DOAS profiles and boxlayer estimations and concludes the paper, suggesting directions for future research.

2 Overview of Similar Studies

While numerous studies have analysed tomographic DOAS to different extend, none has used a fully Bayesian approach to reconstruct NO_2 fields. Recent studies by Hartl (2007); Laepple et al. (2004); Pundt et al. (2005); and Pundt (2006) mostly use discretized local basis functions as reconstruction approach. The inversion methods are typically linear least squares methods with regularization. The error analysis is often based on numerical studies, meaning that extensive simulations with test distributions are made to assess the error metrics.

Hartl (2007) presents a comprehensive analysis of tomographic inversion problems, comparing traditional least squares methods with a fully statistical approach. The dissertation demonstrates that under specific conditions–namely, a Gaussian prior distribution and a linear forward model the maximum a posteriori (MAP) estimate from the Bayesian approach is mathematically equivalent to the solution obtained from the regularized least squares method. Specifically, for a linear forward model $\mathbf{A}$ and measurements $\mathbf{d}$, the least squares solution with Tikhonov regularization is given by:

$$\hat{\mathbf{x}}_{LS} = (\mathbf{R}^T\mathbf{R} + \lambda\mathbf{L}^T\mathbf{L})^{-1}\mathbf{R}^T\mathbf{d} \tag{1}$$

where λ is the regularization parameter and $\mathbf{L}$ is the regularization matrix. In the Bayesian framework, assuming a Gaussian prior with covariance $\mathbf{B}$ and measurement error covariance $\mathbf{N}$, the maximum a posteriori (MAP) estimate is according to Rodgers (2000):

$$\hat{\mathbf{x}}_{MAP} = (\mathbf{R}^T\mathbf{N}^{-1}\mathbf{R} + \mathbf{B}^{-1})^{-1}\mathbf{R}^T\mathbf{R}^{-1}\mathbf{d} \tag{2}$$

These solutions are equivalent when $\mathbf{N} = \sigma^2\mathbf{I}$ and $\mathbf{B}^{-1} = \lambda\mathbf{L}^T\mathbf{L}$. However this requires linearity of the forward model and the prior has to be fully gaussian. It has to be stated that in our forward model the response function of the long-path DOAS is

https://doi.org/10.5194/egusphere-2026-2724
Preprint. Discussion started: 16 June 2026

assumed to be linear, however any statement about positivity of the NO_2 density field makes the prior non-gaussian. Therefore the MAP is not equivalent to the least squares solution for a tomographic long-path DOAS problem.

Hartl (2007) also emphasizes that the primary advantage of the fully statistical approach lies in its ability to provide a comprehensive characterization of uncertainty. While the MAP estimate offers a point solution, the Bayesian method yields the full posterior probability distribution. This distribution enables the calculation of credibility intervals and the true standard deviation of the reconstruction, offering a more nuanced understanding of the solution's reliability. Furthermore, the Bayesian framework allows for the incorporation of more sophisticated prior models, which can capture complex spatial and temporal correlations in the atmospheric state. We will make use of this possibility by employing the correlated field prior model provided by NIFTy.

3 Measurement Techniques and Post-Processing

3.1 Measurement Setup

In this study only the long-path mode of the HyDOAS was used. In total 4 retro-reflectors were set up. There were 3 reflectors at the meteorological tower of the KNMI and one other was placed in a distance of 800m at a shed. The heights of the reflectors at the tower was 2 m, 47 m, 107 m, 207 m. The whole measurement setup is shown in figure 1. The reflector at the shed was at a height of approximately 1 m. Additionally, Two ICAD instruments (Airyx GmbH) were deployed at the KNMI tower: an ICAD NO_2-NOx-NO analyzer (Series 210DL) at 1 m height and an ICAD HONO-NO_2 analyzer (Series 210L) at 27 m height. Both instruments use Iterative Cavity DOAS (ICAD) spectroscopy with effective absorption path lengths of up to 4 km and 3 km respectively, providing direct spectroscopic NO_2 measurements without requiring calibration gases and with sub-0.1 ppb/month zero drift. The NOx analyzer additionally derives NOx and NO via internal NO-to-NO_2 conversion, and was operated at 5 s time resolution; the HONO/NO_2 analyzer simultaneously detects HONO and NO_2 in the 350–390 nm range with no observed cross-sensitivities to water vapor, NOx, or formaldehyde, and was operated at 30 s resolution. Detection limits (2σ, 60 s) are 0.03 ppb for NO_2 (NOx unit), and 0.08 ppb for HONO and 0.16 ppb for NO_2 (HONO/NO_2 unit).

We aim at reconstructing the area between the KNMI tower and the HyDOAS (shaded area in figure 1).

3.2 MAX-DOAS

The Multi-Axis Differential Optical Absorption Spectroscopy (MAX-DOAS) measurements used in this study were performed with a 1D SkySpec instrument (Airyx GmbH, Germany). The instrument was operated at the Cabauw Experimental Site alongside with 32 other MAX-DOAS instrument, among them 13 SkySpec instruments during the CINDI III campaign (Van Roozendael et al., 2025). It was configured and operated in full compliance with the official CINDI III measurement protocol (version 4.1), ensuring consistent geometry, timing, and spectral configuration across all participating instruments.

The instrument performed automated elevation scans in a fixed azimuthal direction of 287° following the standard elevation sequence of $-2°, 1°, 2°, 3°, 4°, 6°, 8°, 15°, 30°, 90°$. Each spectrum was recorded with an integration time of approximately

https://doi.org/10.5194/egusphere-2026-2724
Preprint. Discussion started: 16 June 2026

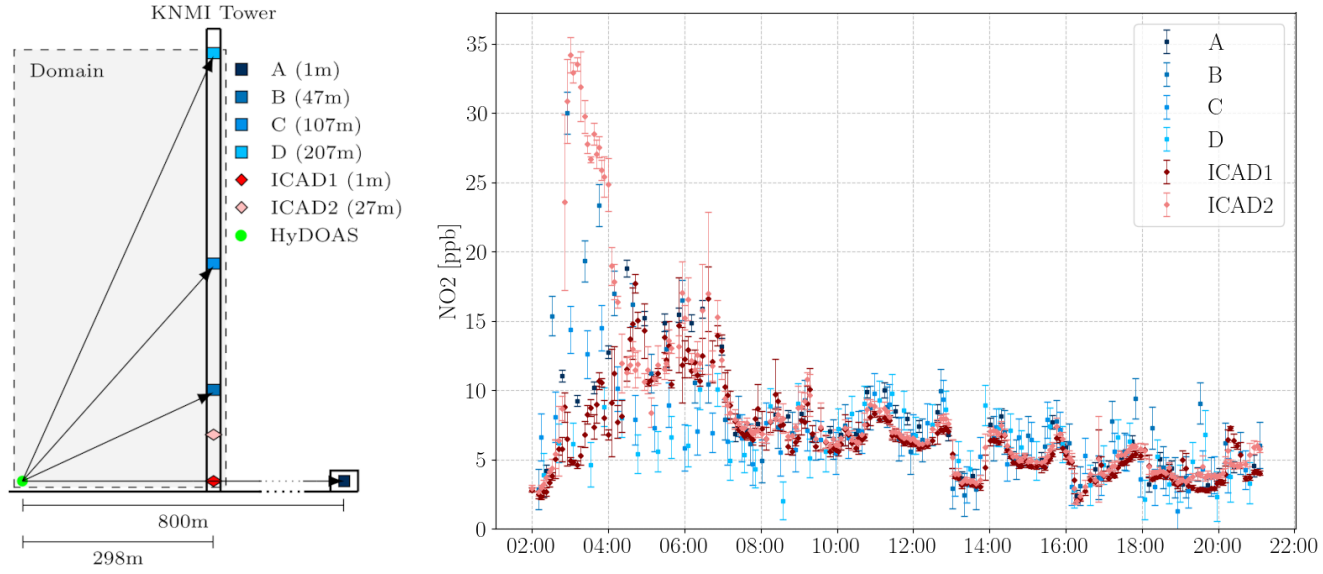

Figure 1. Left: Measurement Setup at the CINDI III measurement site. The distances in round brackets represent the heights of the reflectors and ICAD devices. Right: Ancillary data from the CINDI III campaign of the 18.06.2024 after temporal resampling. The blue scatter points resemble the HyDOAS data and the red points reflect the resampled ICAD data. Errorbars resemble the total measurement error according to equation 3. The inversion at night (03:00 - 04:00) is clearly visible.

one minute. According to the CINDI III schedule, one full elevation sequence was completed every 15 minutes, alternating with zenith sequences to provide continuous temporal coverage between 04:10 and 19:10 UTC. Additional twilight sequences were conducted before sunrise and after sunset, while dark current and offset measurements were performed at the end of each measurement day. A field calibration of all scanning instruments was performed at the campaign site in collaboration with Luftblick Earth Observation Technologies to ensure consistent instrumental response and to find individual exposure times.

The SkySpec spectrometer (AvaSpec ULS2048) covers a wavelength range of 300-460 nm with a spectral resolution of 0.6nm. The detector was temperature-stabilized at around 20 °C. All calibration procedures (dark, offset, and wavelength) followed the standard manufacturer routines. The measurements were stored in a format compliant with the CINDI III and FRM4DOAS data standards.

Differential slant column densities (DSCDs) of NO_2 were retrieved using the CINDI III NO_2 UV analysis window (338-370 nm), including absorption cross-sections of NO_2 (Vandaele et al., 1998), O_3 (Serdyuchenko et al., 2014), O_4 (Finkenzeller and Volkamer, 2022), H_2O (Rothman et al., 2013), and the Ring spectrum (Wagner et al., 2009). A fifth-order polynomial was applied to correct broadband structures, and a daily noon reference spectrum (11:35-11:50 UTC) served as reference. Reference alignment was performed by shift-and-stretch correction relative to this reference.

The retrieved DSCDs were subsequently inverted to vertical NO_2 profiles using the Optimal Estimation Method (OEM) implemented in QDOAS and the M^3 (Munich Multiple wavelength MAX-DOAS) retrieval algorithm (Chan et al., 2020)

https://doi.org/10.5194/egusphere-2026-2724
Preprint. Discussion started: 16 June 2026

developed by RAL and LMU within the CINDI III Profiling Task Team. The retrieval used 100 m layers from the surface up to 4 km altitude, based on mean temperature, pressure, and humidity profiles from De Bilt radiosondes.

A priori NO_2 profiles were exponentially decreasing with altitude (scale height 1 km, total column (9×10^{15}) molec cm^{-2}), with 100% relative uncertainty and a vertical correlation length of 0.2 km. Aerosol extinction profiles were retrieved simultaneously using O_4 DSCDs, applying wavelength-independent optical parameters (single-scattering albedo 0.92, asymmetry parameter 0.68, Ångström exponent 0.92, surface albedo 0.06).

The resulting NO_2 profiles were used as reference data to evaluate the reconstructed NO_2 distributions from the Bayesian inference approach described in Section 4.2.

3.3 Processing of MAX-DOAS Retrievals

MAX-DOAS retrievals under cloudy conditions present significant challenges due to the complexity of light paths in the presence of clouds. The reliability of these retrievals is compromised when the forward model does not account for cloud effects, leading to potential inaccuracies in the derived atmospheric profiles.

For the measurements conducted on 18.06.2024, the presence of extensive cloud cover introduces substantial uncertainty into the MAX-DOAS retrievals. However, it is important to note that the impact of clouds on MAX-DOAS measurements is not uniform across all viewing geometries. Observations at low elevation angles may retain some validity due to their sensitivity to near-surface atmospheric layers, where the influence of clouds is less pronounced as shown by Vlemmix et al. (2015).

However between 10:00 and 21:00 it was raining on that day. Therefore we excluded retrievals after 10:00, since retrievals in cloudy conditions are very challenging and the additional optical interference and altered atmospheric composition during rainfall do not allow for reliable retrievals during this time. Excerpts from precipitation data are shown in Fig. A1. In contrast to the MAX-DOAS measurements, OpenPath and ICAD measurement are not significantly influenced by rainfall.

3.4 Hybrid DOAS

The new HyDOAS instruments are based on a fibre lens telescope ($f = 200$ mm) combined with an Avantes ULS spectrometer (CCD sensor, spectral range 316 - 477 nm, Resolution 0.6 nm FWHM) and a single high-power LED peaking at 450 nm. The instrument has an embedded PC which controls the data acquisition measurement routine and real time DOAS evaluation of the acquired spectra using DOASIS (Kraus, 2006). The 2D motors enable consecutive measurements on multiple reflectors as well as automatic path alignment and correction if necessary. The instrument is able to measure in passive and active mode (MAX-DOAS and long-path DOAS), but for this campaign only the long-path mode was used.

For the measurements at the CINDI Campaign the HyDOAS instrument was set to a time resolution of 30 seconds for a single spectrum acquisition and measured on 4 retro reflectors within a 15 min time window to match the duration of the elevation sequences of the MAX-DOAS instruments. Reference spectra and background spectra – the latter for each retro reflector run – were automatically acquired within the measurement routine. Further, the HyDOAS instruments feature sensors for ambient temperature and pressure for conversion of gas slant column densities to volume mixing ratios. The DOASIS setup for the CINDI data analysis is specified in the appendix.

https://doi.org/10.5194/egusphere-2026-2724
Preprint. Discussion started: 16 June 2026

3.5 Processing of HyDOAS Data

We chose to use HyDOAS and ICAD measurement data from the 18.06.2024 during the CINDI III campaign. Especially on that day there was a pronounced inversion during the night and early morning, which we expect to see represented in the reconstructed field. Additionally, we have access to MAX-DOAS retrievals from this day. The data is shown in Fig. 1.

ICADs and HyDOAS have different measurement times. In this case the ICADs measured in 5 s intervals and the HyDOAS measured 5 times with an integration time of 1 minute to each reflector. While in theory one could reconstruct the NO_2 density field using a 5 s time resolution this would result in short reconstruction periods of 2.5 minutes in total due to computational cost (given a resolution of 78×104 px and 8 GB of VRAM). Since the open-path instrument provides one-minute averages, retaining the native 5 s ICAD resolution would not add temporal information but would drastically increase computational load. Therefore we chose to resample the ICAD values to 5 minute values. The 5 HyDOAS measurements per reflector were also averaged to one value. With 8 GB VRAM we were able to reconstruct time windows of roughly 6 hours. The resulting total measurement error is the sum of the temporal resampling error (standard deviation of the resampled group of measurements) and the mean of the measurement errors.

$$\sigma = \sigma_{resampling} + \sigma_{measurement} \tag{3}$$

The same applies to the ICAD measurements. The handling of reflector A requires a recalculation of the measurement value, since the reflector was situated in a distance of 800 m, but the reconstruction area only covers the distance to the tower (298 m). We recalculate the NO_2 density between the tower and the HyDOAS system as $d'_A = d_A \cdot l_{tower}/l_{shed}$ and also increase the error by the same fraction.

4 Inference Machinery

4.1 Numerical Information Field Theory

The goal of the inference is the retrieval of the spatial distribution of NO_2 densities. Due to the tomographic measurement setup and the noise present in the measurements, this is an ill-posed inverse problem. In order to address this problem, we propose the use of a Bayesian reconstruction. In such a framework, the posterior probability of the quantity of interest (QoI) s given the measured data d is given as:

$$P(s|d) = \frac{P(d|s)P(s)}{P(d)}, \tag{4}$$

where $P(s|d)$ is the posterior probability, $P(d|s)$ the likelihood function, $P(s)$ the prior probability, and $P(d)$ the model evidence (marginal likelihood).

In the scenario discussed here, s is the 3D NO_2 density field. As such, the posterior over such a high dimensional space becomes challenging to analyse. We are interested in expectation values over the posterior, such as the mean density and

https://doi.org/10.5194/egusphere-2026-2724
Preprint. Discussion started: 16 June 2026

standard deviation. Such expectation values over a high dimensional space can be evaluated efficiently with posterior samples:

$$\langle s \rangle_{P(s|d)} = \int s\, P(s|d)\, \mathrm{d}s \tag{5}$$

$$= \sum_{i=0}^{\infty} s_i \quad \text{where} \quad s_i \leftarrow P(s|d). \tag{6}$$

The problem of solving the inverse problem then becomes generating posterior samples.

To obtain these posterior samples we used Geometric Variational Inference (geoVI) embedded in the NIFTy framework (Frank et al., 2021). This algorithm uses Riemannian geometry to construct a coordinate transformation that simplifies complex, non-linear posterior distributions into a form where they can be accurately approximated by a normal distribution.
geoVI requires three main components for the inference:

- A model of the measurement process that maps the QoI s to the data space. This encodes all the relevant physics of the measurement itself.
- A likelihood function on the data space. The likelihood contains information on the noise distribution of the data.
- A generative function g, that maps uniformly gaussian distributed latent variables ξ to the signal space, such that $P(\xi) = \mathcal{G}(\xi, \mathbb{1}),\ s = g(\xi),\ P(\xi)\mathrm{d}\xi = P(s)\mathrm{d}s$. g encodes all the prior knowledge we want to include on s, such as positivity, correlation lengths in space and time, etc.

These components will be developed in section 4.2 and 4.3.

4.2 Likelihood

The forward model maps the spatiotemporal density field $s(x,t)$ to the data space of d and accounts for the specific measurement times and geometries of the HyDOAS and ICAD instruments. Mathematically, this model is expressed as:

$$R : s(x,t) \mapsto \hat{d}(t,j) \tag{7}$$

where $s(x,t)$ is the 2D×1D spatiotemporal density field and $\hat{d}(t,j)$ is the vector of predicted measurement data.

This operator encodes which parts of the field contribute to each measurement and is given by the set of response functions $\{r_j(x)\}$, where j indexes the measurement system.

For each time t, the model computes the predicted measurement which, for HyDOAS, becomes the path integral over s from the instrument position to the reflector:

$$\hat{d}(t,j) = \int r_j(x) s(x,t)\, dx = \int_0^L s(\mathbf{u}(l),t)\, dl \tag{8}$$

where $\mathbf{u}(l) = \mathbf{u}_0 + l\,\hat{\mathbf{n}}$ for $l \in [0, L]$, and $\hat{\mathbf{n}}$ is the unit direction vector between the measurement device's location and the reflector position.

https://doi.org/10.5194/egusphere-2026-2724
Preprint. Discussion started: 16 June 2026

The response of the ICAD on the density field can be expressed as an evaluation of the field at the instrument position:

$$r_j(x) = \delta(x - x_0)$$

where x_0 is the location of the ICAD instrument.

The noise covariance matrix N describes the statistical uncertainty associated with the measurements. Since the HyDOAS and ICAD instruments report independent uncertainties for each individual measurement, and no cross-correlations between measurement errors at different times or between instruments are expected, we assume uncorrelated Gaussian noise. This results in a diagonal covariance structure,

$$N = \mathrm{diag}(\epsilon_1^2, \epsilon_2^2, \ldots, \epsilon_M^2),$$

where ϵ_i denotes the reported standard deviation of the i-th measurement.

With the response function R, the measured data d and the noise covariance N, it is now possible to define the likelihood function:

$$\mathcal{L}(d|s) \propto \exp\left(-\frac{1}{2}(d - R(s))^T N^{-1}(d - R(s))\right) \tag{9}$$

4.3 Prior Model

The prior model encodes our beliefs about the NO_2 density field before observing any measurement data. For physically plausible NO_2 density fields, several requirements must be fulfilled:

1. strict positivity, as negative concentrations are physically impossible
2. spatial smoothness, reflecting the diffusive nature of NO_2 transport in the atmosphere
3. temporal smoothness, as atmospheric NO_2 concentrations evolve continuously
4. realistic amplitudes and variability that match typical NO_2 levels and their fluctuations

We implemented our prior model using the correlated field model provided by NIFTy (Arras et al., 2021, 2022), which constructs statistically homogeneous and isotropic Gaussian processes with flexible power spectra. This hierarchical model acts as the generative function $g(\xi)$ that was introduced in section 4.1. It incorporates several hyperparameters that control the statistical properties of the field. The "mean" parameter sets the typical offset or baseline level of the logarithmic field, which after exponentiation determines the characteristic NO_2 concentration scale. The "fluctuations" parameter controls the overall amplitude of variations around this baseline, governing how much the NO_2 density deviates from its mean value. The "loglogavgslope" parameter specifies the exponent of the power-law component of the power spectrum, determining the correlation length scale: negative slopes favor smoothness by giving more power to large-scale (low-frequency) modes, while less negative slopes allow more small-scale structures. Together, these parameters define a flexible prior that can accommodate both smooth large-scale concentration patterns and localized variations, while the additional "flexibility" and "asperity" parameters

https://doi.org/10.5194/egusphere-2026-2724
Preprint. Discussion started: 16 June 2026

allow for deviations from the pure power-law spectrum. Detailed descriptions of all parameters can be found in the NIFTy user guide (Max-Planck-Society, 2024). Table A1 in the appendix provides the complete parameter configuration used in our reconstruction.

The hyperparameters of the correlated field model (offset, fluctuations, loglogavgslope, flexibility, asperity) are not fixed, but are themselves treated as random variables with their own prior distributions. During the variational inference process, these hyperparameters are optimized jointly with the field reconstruction. This allows the data to inform the correlation structure: for instance, if the measurements indicate stronger spatial correlations than initially assumed, the inference will adapt the local correlation length scale accordingly. The geoVI algorithm updates both the field values and the hyperparameters iteratively, ensuring that the final reconstruction reflects both the prior knowledge and the information content of the observations.

Strict positivity is enforced by applying a softplus transformation

$$f(x) = \ln(1 + e^x) \tag{10}$$

within the prior model, which maps the unconstrained latent field to positive NO_2 densities.

The initial hyperparameter values were chosen to produce temporal NO_2 variability consistent with the ICAD in-situ measurements from the same campaign, which show median 5-min changes of 0.32 ppb during well-mixed conditions and 1.24 ppb during the dynamic inversion period. Since the hyperparameters are inferred jointly with the field during the NIFTy inversion, the prior serves primarily to regularize the solution in data-sparse regions rather than to rigidly fix the fluctuation scale. Figure A2 shows a sample drawn from the prior. The field is strictly positive, spatially and temporally smooth, and exhibits frame-to-frame changes of 0.2–1.2 ppb per 5 min, which is consistent with the observed ICAD variability. The low mean NO_2 concentration level reflects the rural background at Cabauw, while the fluctuation amplitude captures realistic local variability without producing extreme values.

5 Inference- and Validation Methods

To perform the Bayesian inference, we use the variational inference machinery provided by NIFTy - specifically the geoVI algorithm. Instead of yielding a single best-fit field, geoVI returns an approximate posterior distribution from which we draw samples. These posterior samples allow us to estimate the mean $\bar{s}(x,t)$, the standard deviation $\sigma_s(x,t)$, and other statistical quantities of the reconstructed spatiotemporal NO_2 field.

Due to hardware limitations, we split the measurements of the whole day into 3 sections and reconstruct these sections separately. The spatial resolution was 78×104 pixels. Table A2 shows the inference hyperparameters for geoVI.

The quality of these reconstructions was assessed using several metrics: the χ^2 values, the residuals between observed and modeled data, the similarity of the reconstructed density fields across different time sections, and the comparison of 1D height profiles calculated from the 2D reconstructions with MAX-DOAS 1D profiles and boxlayer estimations. We define the χ^2

https://doi.org/10.5194/egusphere-2026-2724
Preprint. Discussion started: 16 June 2026

values as:

$$\chi^2 = \frac{1}{N}\sum_{i=1}^{N}\frac{(\hat{d}_{s,i} - d_i)^2}{\sigma_i^2}$$

where $\hat{d}_s$ is retrieved from the reconstructed field using the response functions described in the likelihood section 4.2. A χ^2 value close to 1 indicates a good fit between the model and data when considering measurement uncertainties: values near 1 show that residuals are consistent with the expected noise level, while values significantly below 1 suggest overestimated uncertainties and values significantly above 1 indicate underestimated uncertainties or systematic model-data mismatches.

As a geometrically simple reference, we compute so-called boxlayer estimates — piecewise-constant concentration layers derived by differencing the path-integrated VCDs between successive reflector heights, under the assumption of horizontal homogeneity. The concentration in layer i is calculated as:

$$C_i = \frac{\left| V_{i+1} \cdot h_{i+1} \cdot \frac{L_{i-1}}{L_i} - V_i \cdot h_i \right|}{h_{i+1} - h_i}, \tag{11}$$

where C_i is the concentration in layer i, V_i is the vertical column density measured to reflector at height h_i, h_i is the height of reflector i and the fraction $\frac{L_{i-1}}{L_i}$ resembles a correction factor to account for the path length difference in two dimensions. In the two-dimensional geometry, the upper paths are longer compared to the lower ones due to the different angles. The fraction $\frac{L_{i-1}}{L_i}$ compensates for this, since otherwise concentrations in upper layers would be overestimated.

6 Numerical Results

We define the resulting mean posterior density field from the sampling process $\bar{s}$ and its standard deviation σ_s. Figure 2 displays the most informative timeslices of the reconstruction $\bar{s}$, revealing several key observations:

1. During the inversion at 03:00, high NO_2 density flares are visible at heights between 10 m and 30 m, consistent with expectations from raw measurement data.

2. Transitions occur at 08:08 and 14:28, coinciding with the start of a new reconstruction time range.

3. Within each of the three reconstruction time windows, the field structure remains temporally coherent.

The χ^2 values of the three reconstructed sections are presented in table 1 and are consistently near 1, indicating that the reconstructed mean density field accurately matches the measurement data within the bounds of their associated errors. The highest χ^2 of 1.9 is in the time range where the inversion takes place, reflecting the high variability on faster timescales than our temporal resolution given by the HyDOAS measurements.

The temporal average of the relative standard deviation in Figure 3 matches our assumptions about the distribution well. We expect low standard deviation in areas where measurement coverage is high – especially at the ICAD positions – and a high standard deviation where we have less measurement coverage. The overall relative standard deviation is high and can exceed

https://doi.org/10.5194/egusphere-2026-2724
Preprint. Discussion started: 16 June 2026

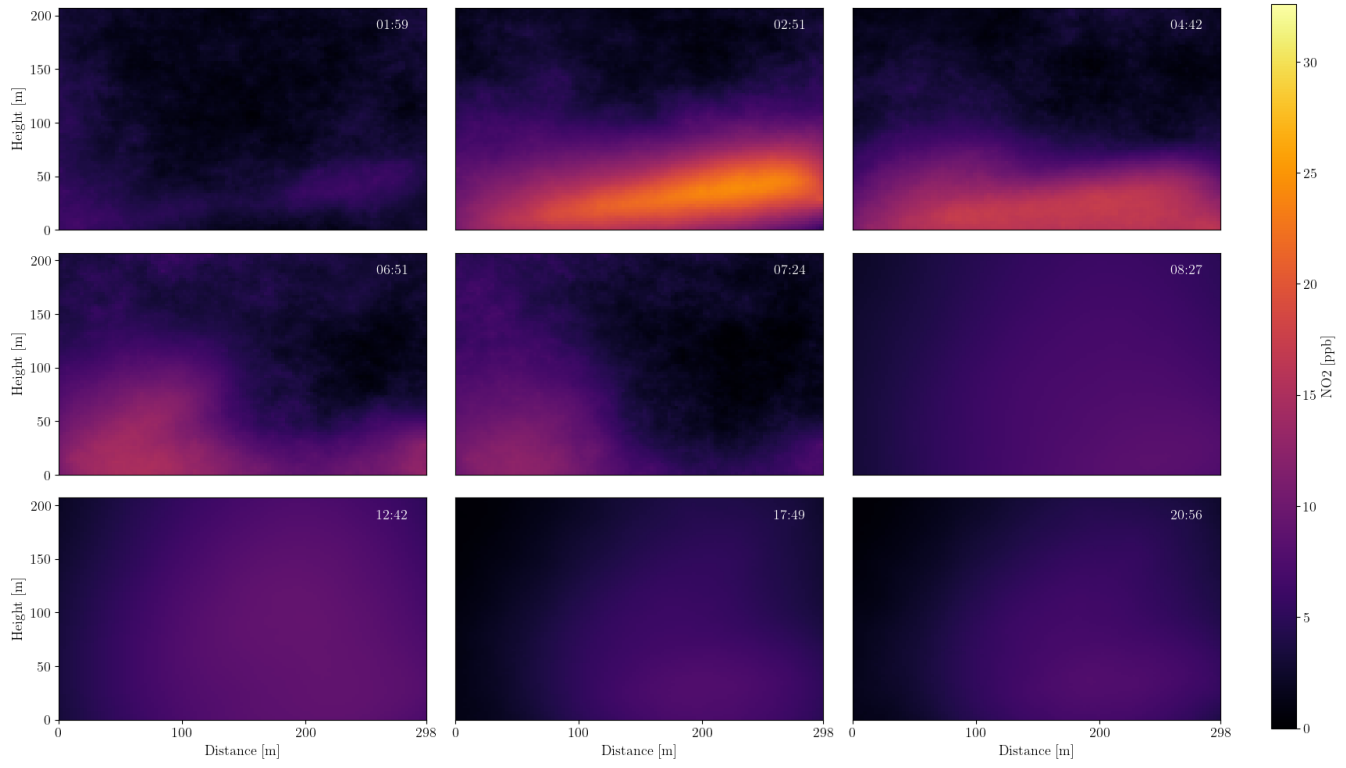

Figure 2. Posterior mean NO_2 density field from the Bayesian spatiotemporal reconstruction shown as consecutive time slices. Each panel represents the reconstructed NO_2 concentration distribution in the vertical plane between the HyDOAS system and the KNMI tower at different times of day. The correlated-field prior enforces physical smoothness in regions with limited measurement coverage, while preserving fine-scale variability near the measurement lines. These two-dimensional fields serve as the physically consistent basis for deriving reliable low-altitude NO_2 profiles.

Time Range	χ^2 Value
01:59:48 - 08:08:20	1.9 ± 0.17
08:22:20 - 14:18:25	1.0 ± 0.01
14:28:07 - 21:04:47	1.2 ± 0.09

Table 1. χ^2 values of reconstructions within the three time ranges. The values are close to 1, indicating a good fit between the reconstructed field and the measurement data when considering the measurement uncertainties.

1.0 especially at the top left corner. This is to be expected since the light path coverage is low in that region. The lowest relative uncertainty is where the ICADs are positioned and in the bottom center of the domain. In the most informed regions the relative uncertainty is between 0.1 and 0.4.

https://doi.org/10.5194/egusphere-2026-2724
Preprint. Discussion started: 16 June 2026

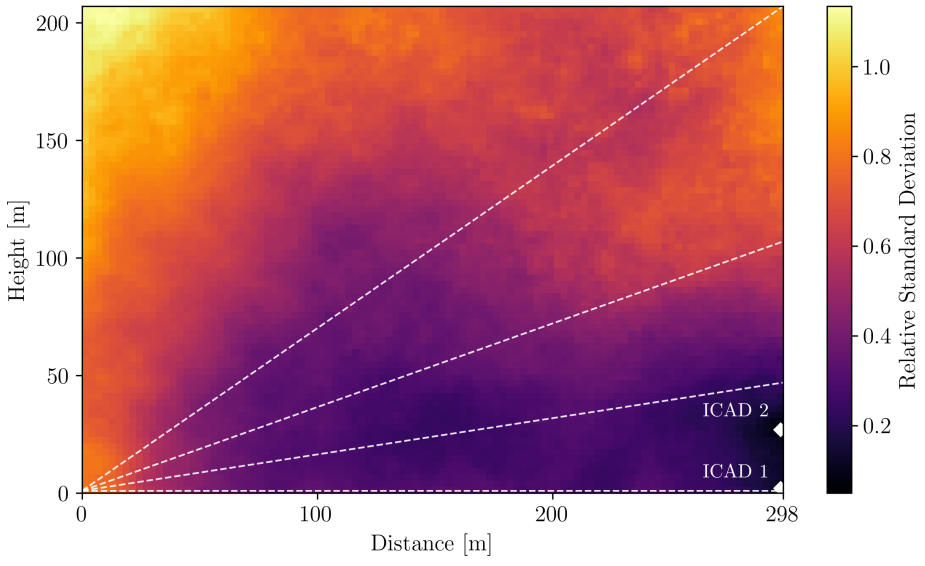

Figure 3. Mean of the relative standard deviation over all timeslices. Lower values (black-purple) indicate regions strongly constrained by the HyDOAS and ICAD measurements, while higher values (yellow-red) mark areas dominated by the prior due to limited ray-path coverage. The positions of the two ICAD in-situ sensors and the HyDOAS light paths are shown for reference. This map highlights the effective information content and spatial sensitivity of the Bayesian reconstruction.

We calculate the 1D averaged height distribution by averaging the posterior mean $\bar{s}$ and σ_s over the horizontal axis. The resulting profiles are shown as a heatmap in the appendix (Figure A3). Noticeable is that, between the time ranges at those times where we had to cut data to fit our hardware limitations (08:08 and 14:18), the transitions are not smooth. An explanation for this is, that, since the three time ranges do not have access to measurement information in the other time ranges, their correlated field models will have slightly different hyperparameters after the inference. We can see from the relative standard deviation discussed before that in height the uncertainty increases up to roughly 0.8. Therefore deviations within the standard deviation are to be expected, especially at higher altitudes. In lower altitudes the profiles at the time range transitions match well.

Figure 4 shows excerpts from the comparisons at times 06:14, 06:59 and 09:44. Notice that the NIFTy reconstruction puts more emphasis on the ICAD measurements which is intuitively reasonable since their measurement error is much smaller than the HyDOAS measurements and the measurement density at their location is higher. Most of the time, the vertical distribution of the calculated boxlayers agrees well with the reconstructed profiles and are always within the boxlayer errors. The elevated boxlayer 3 value observed at 06:14 appears to be an outlier, likely due to the violation of the no-horizontal-change assumption in this instance. This anomaly suggests that significant horizontal variability in NO_2 concentration occurred at that time, challenging the underlying model assumptions and potentially leading to the overestimation in the upper layer. The 2D reconstructions in Fig. 2 supports this hypothesis. The MAX-DOAS retrievals have to be interpreted with caution. Since the

https://doi.org/10.5194/egusphere-2026-2724
Preprint. Discussion started: 16 June 2026

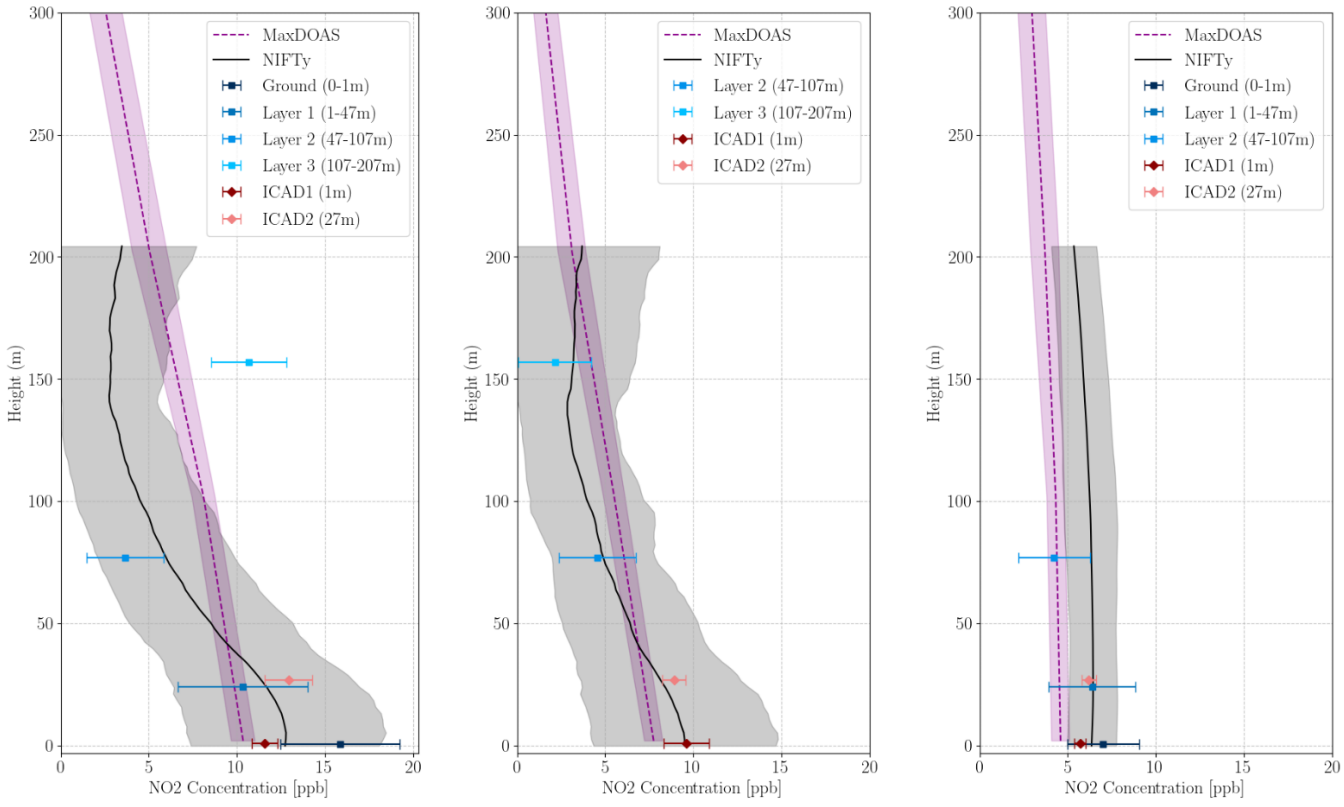

Figure 4. Comparison of 1D height profiles calculated from the NIFTy reconstruction (black), the MAX-DOAS measurements (purple) and the boxlayers (blue) for selected times during the early morning of 18.06.2024 for 06:14 (left), 06:59 (center) and 09:44 (right). The ICAD measurements are also highlighted in red. The comparison illustrates the temporal evolution of the near-surface NO_2 layer and demonstrates that the profiles inferred from the Bayesian 2D fields are consistent with established retrievals within their respective uncertainties.

day was cloudy the real uncertainties are probably higher than estimated by the retrieval algorithm. However the profiles show the same features as the boxlayers and the NIFTy height profiles.

To quantify the accuracy of the NIFTy approach, an intercomparison of the three profiles is conducted. This involves calculating the average absolute and relative distance between the mean values of the NIFTy reconstruction, the MAX-DOAS retrieval and the boxlayer estimations:

Comparison	abs diff. NO_2	rel. diff. NO_2
Boxlayers - MAX-DOAS	2.69 ppb	32.33 %
Boxlayers - NIFTy	1.82 ppb	14.86 %
MAX-DOAS - NIFTy	2.11 ppb	29.38 %

Table 2. Intercomparison of the absolute and relative differences between the different profile retrieval methods.

https://doi.org/10.5194/egusphere-2026-2724
Preprint. Discussion started: 16 June 2026

7 Outlook and Conclusions

In the previous sections we demonstrated the feasibility of retrieving vertical NO_2 profiles from sparse, geometrically constrained measurements using a Bayesian spatiotemporal reconstruction framework. By reconstructing 2+1D NO_2 density fields as an intermediate step, we successfully derived physically consistent height profiles from combined HyDOAS and ICAD measurements during the CINDI-III campaign. The reconstructed fields exhibit temporal coherence, reproduce key atmospheric features such as the nocturnal inversion layer, and yield vertical profiles that agree with boxlayer estimates and independent MAX-DOAS retrievals within their respective uncertainties. The mean absolute differences between NIFTy profiles and comparison methods (1.82-2.69 ppb) indicate reasonable consistency, while the χ^2 values near unity confirm that the Bayesian approach successfully reconciles measurement data with their reported uncertainties. In the following, we assess the agreement between the different retrieval methods and discuss key limitations arising from the measurement geometry.

The geometry of the experiment inherently limits the information content of the data. All light paths lie nearly in one vertical plane connecting the HyDOAS emitter and the KNMI tower, creating a largely symmetric setup.

This symmetry causes the reconstructions to be more reliable in the vertical than in the horizontal direction, with lateral smoothing controlled primarily by the prior correlation length. The observed smooth horizontal gradients in the posterior mean fields (Figure 2) thus reflect prior-driven regularization rather than measurement-driven features. Future experiments using additional reflectors at oblique angles creating crossing measurement paths could break this symmetry and improve spatial distinctiveness.

The NIFTy approach produces results that are more consistent with the boxlayers estimation, while showing moderate absolute differences from MAX-DOAS retrievals. The relative differences of 14.86 % - 32.33 % suggest that there are still significant variations between these methods in estimating NO_2 concentrations, however the boxlayer estimations assume no horizontal change in NO_2 and the MAX-DOAS retrieval is influenced by clouds, has only two anchor points within 200 m from the ground and averages over much larger distances (10 km) compared to the HyDOAS measurements ($\sim$ 300 m). Considering these limitations and the internal consistency checks of the χ^2 metric, we find, that the Bayesian framework is capable of reconstructing the NO_2 dynamics using long path DOAS and point measurement data within the confidence interval given by the standard deviation of the reconstruction.

Overall, the Bayesian inference method successfully reconstructs the spatiotemporal evolution of NO_2 within the constraints of a nearly symmetric measurement geometry. Despite limited angular coverage, the inferred fields reproduce vertical gradients observed by MAX-DOAS and boxlayer models within their respective uncertainties. The correlated-field prior ensures physical plausibility where data coverage is sparse, while remaining sensitive to the HyDOAS measurements and especially the high-precision ICAD anchors. These results demonstrate the feasibility of Bayesian inference for atmospheric tomography and motivate future setups with less symmetric geometries to fully exploit the method's potential.

In future studies, we aim to expand the application of this reconstruction method by incorporating data from additional HyDOAS devices and more reflectors. This will enhance the spatial coverage and robustness of the reconstructions. Furthermore, point measurement devices such as ICAD could be utilized as independent validation tools to confirm the accuracy of the re-

https://doi.org/10.5194/egusphere-2026-2724
Preprint. Discussion started: 16 June 2026

constructions. In this study, the limited number of measurements required us to use all available data to probe the NO_2 density field, which unfortunately made direct validation of the 2D reconstructions impossible. Expanding the measurement network will address this limitation and improve confidence in the results.

The combination of long-path DOAS data with MAX-DOAS measurements also holds great potential. Since the HyDOAS system can also operate as a MAX-DOAS instrument, developing an intelligent instrument control algorithm could further optimize information gain. This would allow reconstructions to directly yield high-resolution vertical profiles in two or three dimensions, offering deeper insights into atmospheric dynamics.

Finally, we aim to conduct future studies with improved computational resources, particularly hardware with greater VRAM capacity. This would enable us to reconstruct larger time slices and achieve higher spatial and temporal resolutions while increasing sample size. A larger sample size is particularly beneficial for improving the mean estimation and uncertainty quantification through geoVI.

By addressing these areas, we anticipate that applying the Bayesian method to DOAS tomography will become a powerful tool for understanding urban air quality dynamics and informing air pollution mitigation strategies.

Acknowledgements. We are particularly grateful to Zeqing Chen for her substantial contributions to the MAX-DOAS instrument operation and data analysis during the CINDI-III campaign, without which the comparison presented in this study would not have been possible. We would like to thank Airyx GmbH for their on-site support and maintenance of the HyDOAS instrument. We also express our sincere gratitude to the CINDI-3 organizing team for the excellently managed campaign and for providing decentralized access to all measurement data.

Financial support. We gratefully acknowledge the ESA FRM4DOAS 2.0 project with contract number 4000135355/21/I-DT-lr for the financial support.

Code availability. The NIFTy inference framework is available at https://gitlab.mpcdf.mpg.de/ift/nifty (Edenhofer et al., 2024). Analysis scripts are available from the corresponding author upon reasonable request.

Data availability. HyDOAS, MAX-DOAS and ICAD measurement data from the CINDI-III campaign are available from the corresponding author upon reasonable request.

Author contributions. M.H. developed the Bayesian reconstruction framework, performed the data analysis, and wrote the manuscript. P.H. assisted with the NIFTy implementation and parameter tuning. D.P.,S.S. and J.L. were responsible for ICAD and HyDOAS Instrument

https://doi.org/10.5194/egusphere-2026-2724
Preprint. Discussion started: 16 June 2026

operation during CINDI campaign and reviewed the manuscript. J.L. analyzed the ICAD data. S.S. analyzed the HyDOAS data. M.W. supervised the project and provided feedback on the manuscript.

Competing interests. S.S., J.L., and D.P. are employees of Airyx GmbH, which manufactures the HyDOAS and ICAD instruments used in this study. The remaining authors declare no competing interests.

https://doi.org/10.5194/egusphere-2026-2724
Preprint. Discussion started: 16 June 2026

References

Arras, P., Baltac, M., Ensslin, T. A., Frank, P., Hutschenreuter, S., Knollmueller, J., Leike, R., Newrzella, M.-N., Platz, L., Reinecke, M., and Stadler, J.: NIFTy5: Numerical Information Field Theory v5, ascl:1903.008, 2019.

Arras, P., Bester, H. L., Perley, R. A., Leike, R., Smirnov, O., Westermann, R., and Ensslin, T. A.: Comparison of classical and Bayesian imaging in radio interferometry. Cygnus A with CLEAN and resolve, Astronomy and Astrophysics, 646, A84, https://doi.org/10.1051/0004-6361/202039258, 2021.

Arras, P., Frank, P., Haim, P., Knollm"uller, J., Leike, R., Reinecke, M., and Ensslin, T.: Variable structures in M87* from space, time and frequency resolved interferometry, Nature Astronomy, 6, 259–269, https://doi.org/10.1038/s41550-021-01548-0, 2022.

Bengtsson, L., Andrae, U., Aspelien, T., Batrak, Y., Calvo, J., de Rooy, W., Gleeson, E., Hansen-Sass, B., Homleid, M., Hortal, M., Ivarsson, K.-I., Lenderink, G., Niemelä, S., Nielsen, K. P., Onvlee, J., Rontu, L., Samuelsson, P., Muñoz, D. S., Subias, A., Tijm, S., Toll, V., Yang, X., and Ødegaard Køltzow, M.: The HARMONIE–AROME Model Configuration in the ALADIN–HIRLAM NWP System, Monthly Weather Review, 145, 1919 – 1935, https://doi.org/10.1175/MWR-D-16-0417.1, 2017.

Chan, K. L., Wiegner, M., van Geffen, J., De Smedt, I., Alberti, C., Cheng, Z., Ye, S., and Wenig, M.: MAX-DOAS measurements of tropospheric NO_2 and HCHO in Munich and the comparison to OMI and TROPOMI satellite observations, Atmospheric Measurement Techniques, 13, 4499–4520, https://doi.org/10.5194/amt-13-4499-2020, 2020.

Edenhofer, G., Frank, P., Roth, J., Leike, R. H., Guerdi, M., Scheel-Platz, L. I., Guardiani, M., Eberle, V., Westerkamp, M., and Enßlin, T. A.: Re-Envisioning Numerical Information Field Theory (NIFTy.re): A Library for Gaussian Processes and Variational Inference, Journal of Open Source Software, 9, 6593, https://doi.org/10.21105/joss.06593, 2024.

Faustini, A., Rapp, R., and Forastiere, F.: Nitrogen dioxide and mortality: review and meta-analysis of long-term studies, European Respiratory Journal, 44, 744–753, https://doi.org/10.1183/09031936.00114713, 2014.

Finkenzeller, H. and Volkamer, R.: O2–O2 CIA in the gas phase: Cross-section of weak bands, and continuum absorption between 297–500 nm, Journal of Quantitative Spectroscopy and Radiative Transfer, 279, 108 063, https://doi.org/https://doi.org/10.1016/j.jqsrt.2021.108063, 2022.

Frank, P., Leike, R., and Enßlin, T. A.: Geometric Variational Inference, Entropy, 23, https://doi.org/10.3390/e23070853, 2021.

Hartl, A.: Tomographic Reconstruction of 2-D Atmospheric Trace Gas Distributions from Active DOAS Measurements, Dissertation, Faculty of Physics and Astronomy, Ruprecht-Karls-Universität Heidelberg, https://doi.org/10.11588/heidok.00007173, 2007.

Horbanski, M., Pöhler, D., Lampel, J., and Platt, U.: The ICAD (iterative cavity-enhanced DOAS) method, Atmospheric Measurement Techniques, 12, 3365–3381, https://doi.org/10.5194/amt-12-3365-2019, 2019.

Knollmüller, J. and Enßlin, T. A.: Metric Gaussian Variational Inference, https://arxiv.org/abs/1901.11033, 2020.

Kraus, S. G.: DOASIS: A Framework Design for DOAS, Dissertation, University of Mannheim, ISBN 978-3-8322-5452-0, 2006.

Laepple, T., Knab, V., Mettendorf, K.-U., and Pundt, I.: Longpath DOAS tomography on a motorway exhaust gas plume: numerical studies and application to data from the BAB II campaign, Atmospheric Chemistry and Physics, 4, 1323–1342, https://doi.org/10.5194/acp-4-1323-2004, 2004.

Max-Planck-Society: Getting Started with NIFTy: Correlated Fields, https://ift.pages.mpcdf.de/nifty/user/nifty_cl_getting_started_4_CorrelatedFields.html, accessed: 06.12.2025, 2024.

Platt, U. and Stutz, J.: Differential optical absorption spectroscopy, Physics of Earth and Space Environments, Springer, Berlin, Germany, 2008 edn., https://doi.org/https://doi.org/10.1007/978-3-540-75776-4, 2008.

https://doi.org/10.5194/egusphere-2026-2724
Preprint. Discussion started: 16 June 2026

Pundt, I.: DOAS tomography for the localisation and quantification of anthropogenic air pollution, Analytical and Bioanalytical Chemistry, 385, 18–21, https://doi.org/10.1007/s00216-005-0205-4, 2006.

Pundt, I., Mettendorf, K.-U., Laepple, T., Knab, V., Xie, P., Lösch, J., Friedeburg, C., Platt, U., and Wagner, T.: Measurements of trace gas distributions using Long-path DOAS-Tomography during the motorway campaign BAB II: experimental setup and results for NO2, Atmospheric Environment, 39, 967–975, https://doi.org/https://doi.org/10.1016/j.atmosenv.2004.07.035, 2005.

Rodgers, C. D.: Inverse Methods for Atmospheric Sounding: Theory and Practice, https://doi.org/10.1142/3171, 2000.

Rothman, L., Gordon, I., Babikov, Y., Barbe, A., Chris Benner, D., Bernath, P., Birk, M., Bizzocchi, L., Boudon, V., Brown, L., Campargue, A., Chance, K., Cohen, E., Coudert, L., Devi, V., Drouin, B., Fayt, A., Flaud, J.-M., Gamache, R., Harrison, J., Hartmann, J.-M., Hill, C., Hodges, J., Jacquemart, D., Jolly, A., Lamouroux, J., Le Roy, R., Li, G., Long, D., Lyulin, O., Mackie, C., Massie, S., Mikhailenko, S., Müller, H., Naumenko, O., Nikitin, A., Orphal, J., Perevalov, V., Perrin, A., Polovtseva, E., Richard, C., Smith, M., Starikova, E., Sung, K., Tashkun, S., Tennyson, J., Toon, G., Tyuterev, V., and Wagner, G.: The HITRAN2012 molecular spectroscopic database, Journal of Quantitative Spectroscopy and Radiative Transfer, 130, 4–50, https://doi.org/https://doi.org/10.1016/j.jqsrt.2013.07.002, hITRAN2012 special issue, 2013.

Seinfeld, J. H. and Pandis, S. N.: Atmospheric chemistry and physics, Wiley-Blackwell, Hoboken, NJ, 3 edn., 2016.

Selig, M., Bell, M. R., Junklewitz, H., Oppermann, N., Reinecke, M., Greiner, M., Pachajoa, C., and Ensslin, T. A.: NIFTY - Numerical Information Field Theory. A versatile PYTHON library for signal inference, Astronomy & Astrophysics, 554, A26, https://doi.org/10.1051/0004-6361/201321236, 2013.

Serdyuchenko, A., Gorshelev, V., Weber, M., Chehade, W., and Burrows, J. P.: High spectral resolution ozone absorption cross-sections Part 2: Temperature dependence, Atmospheric Measurement Techniques, 7, 625–636, https://doi.org/10.5194/amt-7-625-2014, 2014.

Steininger, T., Dixit, J., Frank, P., Greiner, M., Hutschenreuter, S., Knollmüller, J., Leike, R., Porqueres, N., Pumpe, D., Reinecke, M., vSraml, M., Varady, C., and Ensslin, T.: NIFTy 3 - Numerical Information Field Theory: A Python Framework for Multicomponent Signal Inference on HPC Clusters, Annalen der Physik, 531, 1800 290, https://doi.org/10.1002/andp.201800290, 2019.

Van Roozendael, M., Apituley, A., Kreher, K., Alves Gouveia, D., Cede, A., Friß, U., Friedrich, M. M., Spinei Lind, E., Merlaud, A., Piters, A., Richter, A., Tack, F., Wagner, T., and Ziegler, S.: Overview of the Third Cabauw Intercomparison of UV-Vis DOAS instruments (CINDI-3), in: EGU General Assembly 2025, Vienna, Austria, https://doi.org/10.5194/egusphere-egu25-13109, eGU25-13109, 2025.

Vandaele, A., Hermans, C., Simon, P., Carleer, M., Colin, R., Fally, S., Mérienne, M., Jenouvrier, A., and Coquart, B.: Measurements of the NO2 absorption cross-section from 42 000 cm-1 to 10 000 cm-1 (238–1000 nm) at 220 K and 294 K, Journal of Quantitative Spectroscopy and Radiative Transfer, 59, 171–184, https://doi.org/https://doi.org/10.1016/S0022-4073(97)00168-4, atmospheric Spectroscopy Applications 96, 1998.

Vlemmix, T., Eskes, H. J., Piters, A. J. M., Schaap, M., Sauter, F. J., Kelder, H., and Levelt, P. F.: MAX-DOAS tropospheric nitrogen dioxide column measurements compared with the Lotos-Euros air quality model, Atmospheric Chemistry and Physics, 15, 1313–1330, https://doi.org/10.5194/acp-15-1313-2015, 2015.

Voigt, S., Orphal, J., and Burrows, J.: The temperature and pressure dependence of the absorption cross-sections of NO2 in the 250-800 nm region measured by Fourier-transform spectroscopy, Journal of Photochemistry and Photobiology A: Chemistry, 149, 1–7, https://doi.org/https://doi.org/10.1016/S1010-6030(01)00650-5, 2002.

Volkamer, R., Spietz, P., Burrows, J., and Platt, U.: High-resolution absorption cross-section of glyoxal in the UV-vis and IR spectral ranges, Journal of Photochemistry and Photobiology A: Chemistry, 172, 35–46, https://doi.org/https://doi.org/10.1016/j.jphotochem.2004.11.011, 2005.

https://doi.org/10.5194/egusphere-2026-2724
Preprint. Discussion started: 16 June 2026

Wagner, T., Deutschmann, T., and Platt, U.: Determination of aerosol properties from MAX-DOAS observations of the Ring effect, Atmospheric Measurement Techniques, 2, 495–512, https://doi.org/10.5194/amt-2-495-2009, 2009.

WHO: WHO global air quality guidelines: particulate matter (PM2.5 and PM10), ozone, nitrogen dioxide, sulfur dioxide and carbon monoxide, World Health Organization, Genève, Switzerland, 2021.

https://doi.org/10.5194/egusphere-2026-2724
Preprint. Discussion started: 16 June 2026

Appendix A

HyDOAS data analysis with DOASIS XS

- NO_2 Voigt et al. (2002) (`NO2_Voigt_293k1000mbar_2002_air`)
- H_2O Rothman et al. (2013) (`H2O_20130919hitran2012_h2o-300-800-ground2_wc20_293_air`)
- Glyoxal Volkamer et al. (2005) (`Glyoxal_Volkamer_2005_296K_0.001nm`)
- Spectral fit range adapted to LED light source
  - 432.6 - 449.8 nm
  - Polynomial order 3
  - High pass filter iterations: 1000

Initial Hyperparameters for the Correlated Field Model

Parameter	Distribution	Mean	Variance
Mean offset	Normal	1	0.5^2
Offset fluct.	Normal	0	0.1^2
Spatial spectral index	Normal	-4.0	0.2^2
Spatial fluct. amplitude	Normal	0.001	0.001^2
Spatial flexibility	Normal	0.2	0.1^2
Temporal spectral index	Normal	-2.5	0.8^2
Temporal fluct. amplitude	Normal	0.2	0.1^2
Temporal flexibility	Normal	2	1^2

Table A1. Initial hyperparameters and their prior distributions for the correlated field model. The notation $\mu \pm \sigma$ indicates a normal distributed prior with mean μ and width σ^2. These values are adapted during the variational inference.

https://doi.org/10.5194/egusphere-2026-2724
Preprint. Discussion started: 16 June 2026

VI Settings

Parameter	Value
VI Iterations	25
Amount of samples	6
Tolerance	10^{-5}
max. linear iterations	100
max. nonlinear iterations	5
max. KL iterations	35

Table A2. Settings for geoVI

Weather conditions during the 18.06.2024

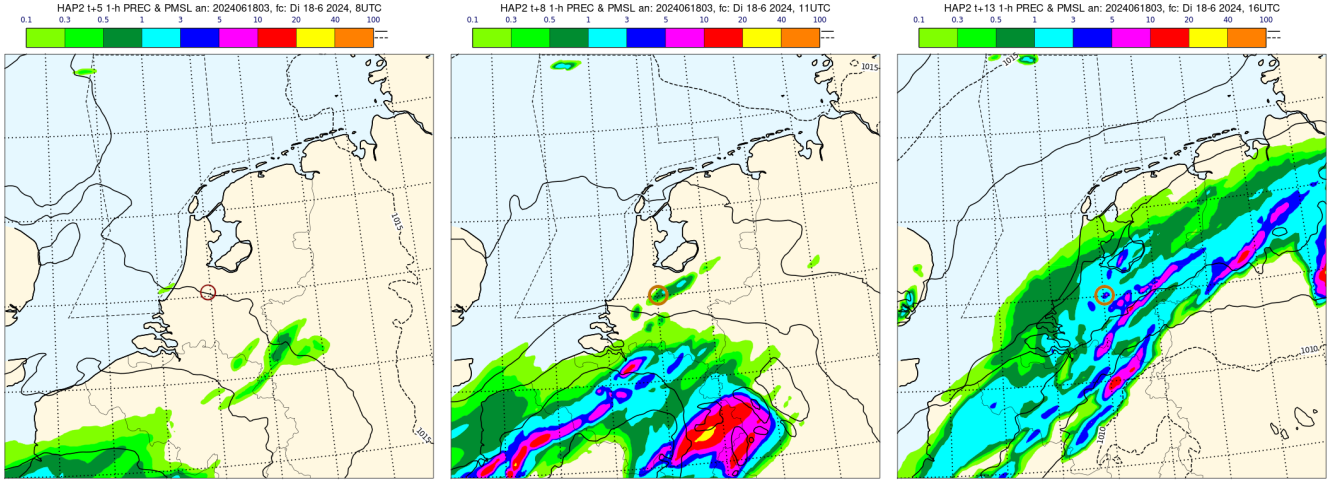

Figure A1. Excerpts from precipitation data over the netherlands from 18.06.2024 using the HARMONIE-AROME model (Bengtsson et al., 2017). Left: 08:00 UTC, Middle: 11:00 UTC, Right: 16:00 UTC. The red spot marks the measurement site at Cabauw.

https://doi.org/10.5194/egusphere-2026-2724
Preprint. Discussion started: 16 June 2026

Prior samples of the correlated field model

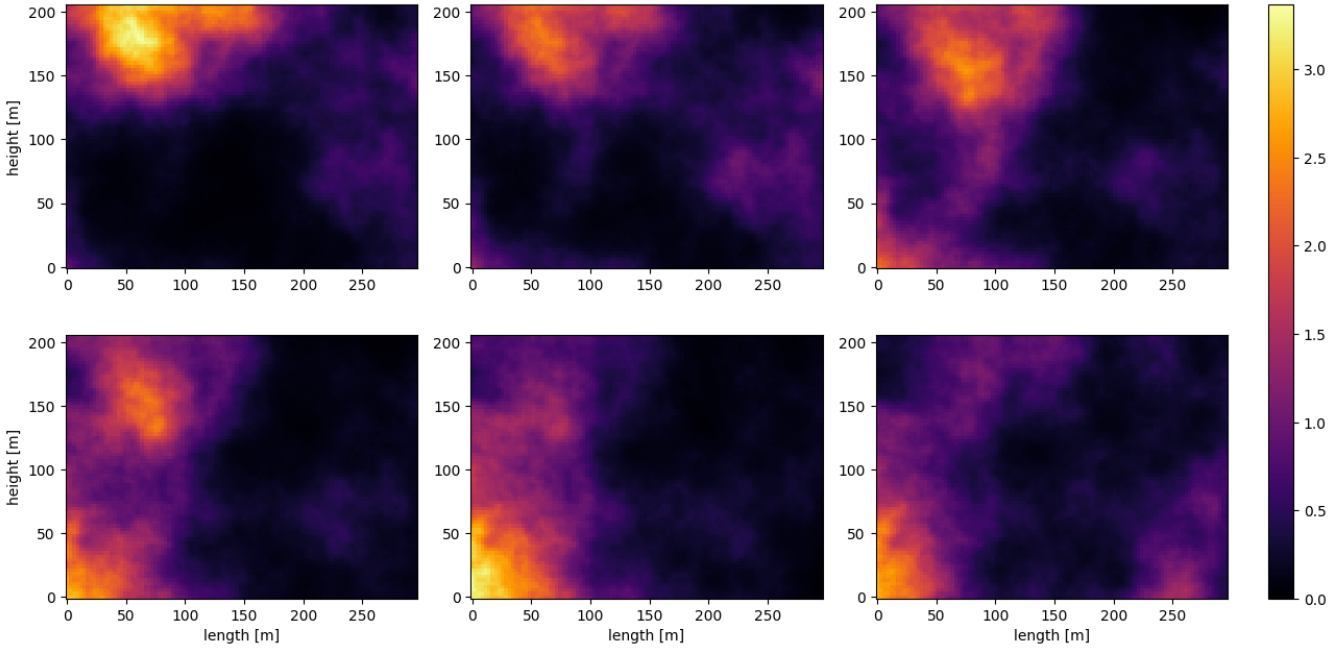

Figure A2. 2×1D sample of the prior correlated field model. The 2D fields shown in the figure are timeslices with increasing time from top left to bottom right. The time between the slices is 5 minutes and the pixel values reflect ppb NO_2.

https://doi.org/10.5194/egusphere-2026-2724
Preprint. Discussion started: 16 June 2026

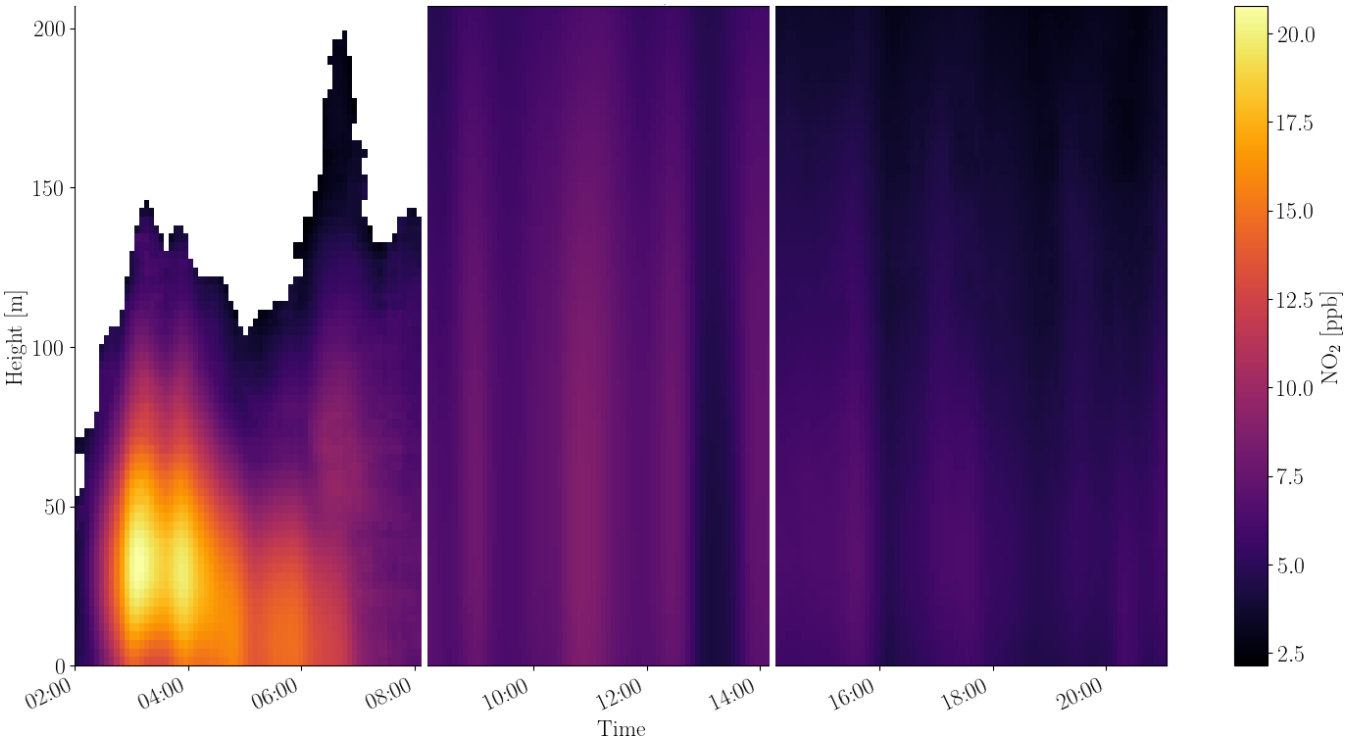

Figure A3. Heatmap generated from the 1D height profiles by averaging the NIFTy reconstruction along the horizontal distance for the 3 time windows (01:59:48 - 08:08:20, 08:22:20 - 14:18:25, and 14:28:07 - 21:04:47). White pixels indicate regions excluded from the average: voxels where the relative posterior standard deviation exceeds 0.9 are masked prior to averaging, and height bins for which fewer than 10 valid horizontal pixels remain after masking are set to `NaN`. The white pixels at elevated heights visible in the first time window therefore reflects the low measurement coverage at altitude, where the sparse light-path geometry leaves the reconstruction prior-dominated and the relative uncertainty consistently exceeds the threshold. When the dynamic of the NO_2 field is less quick, the standard deviation is lower, which is why in the second and third time window the profiles are more complete. The transition between the time windows is due to the fact that they were reconstructed separately, which leads to different hyperparameters of the correlated field model and therefore different uncertainty levels. The heatmap illustrates the temporal evolution of the vertical NO_2 distribution, with higher concentrations near the surface during nighttime and a gradual decrease in concentration with height as the day progresses.